

Ultra-thin surface chemical bonded polyanionic group for 4.7 V LiCoO₂

Xinghua Tan^{a,b,1}, Zhongxing Xu^{a,1}, Zhefeng Chen^{a,1}, Yutao Niu^b, Haoyu Xue^a, Xinghan Chen^a,
Shenyang Xu^a, Yongzhi Liang^a, Xulin Mu^b, Shunning Li^a, Tongchao Liu^{c,*}, Jing Xia^{d,*},
Chunyang Wang^{b,*}, Feng Pan^{a,*}

^a School of Advanced Materials, Peking University, Shenzhen Graduate School, Shenzhen 518055, PR China

^b Shenyang National Laboratory for Materials Science, Institute of Metal Research, Chinese Academy of Sciences, Shenyang 110016, PR China

^c Chemical Sciences and Engineering Division, Argonne National Laboratory, Lemont, IL, USA

^d Key Laboratory of Photochemical Conversion and Optoelectronic Materials, Technical Institute of Physics and Chemistry, Chinese Academy of Sciences, Beijing 100190, PR China

ARTICLE INFO

Keywords:

Surface-bonded SO₄ tetrahedron
High-voltage LiCoO₂
Atomic thickness coating layer
Lithium-ion batteries
Interfacial issues

ABSTRACT

Elevating the charging cut-off voltage is one of the most effective methods to boost the energy density of lithium-ion batteries utilizing a LiCoO₂ (LCO) cathode. However, severe interfacial issues and structural degradation impede the practical application of high-voltage LCO. Here, we develop a surface SO₄ tetrahedron modification strategy to stable the LCO at high voltages. The surface SO₄ tetrahedrons were constructed from under-coordinated oxygen ions on the LCO surface during the reaction with SO₂, thereby enhancing the stability of surface oxygen (bonding effect). More importantly, the surface SO₄ tetrahedron significantly reduced the adsorption energy of ethylene carbonate (EC) on the LCO surface, thereby decreasing the likelihood of nucleophilic attack and oxidation (shielding effect). Owing to the shielding and bonding effects of the surface SO₄ tetrahedron, the interfacial electrochemistry and chemistry of the cathode were regulated. When this strategy was applied to a Mg&Ce-doped LCO, the modified materials (LCO-MC+S) demonstrated remarkable cycling performance, showing 84 % capacity retention after 1000 cycles at 3.0–4.6 V and 80 % after 200 cycles at 3.0–4.7 V. This study proposes a new approach to addressing the instability of high-voltage layered cathode materials.

1. Introduction

With the rapid advancement of portable devices and electric vehicles, there is a growing demand for lithium-ion batteries with higher energy density and longer lifespans [1–4]. The energy density of lithium-ion batteries is directly proportional to the product of practical capacity and output voltage [5]. Therefore, elevating the working voltage to extract more lithium ions from cathode is one of the most straightforward strategies to increase the energy density [6]. For example, the dominant cathode of battery used in 3C electronic devices, LiCoO₂ (LCO), reaches a specific capacity of 220 mAh g⁻¹ when the cut-off voltage is increased from 4.3 V (corresponding to 140 mAh g⁻¹) to 4.6 V [7]. However, operating at such high voltages (≥4.6 V) pose great challenges, including aggressive interfacial issues and structure degradations [8,9].

The accelerated interfacial issues, including surface side reactions [10] and oxygen evolution [11], lead to rapid capacity fade and reduced Coulombic efficiency [12]. Due to extensive efforts, the mechanism underlying the interfacial issues on the high-voltage cathodes is relatively clear [13–15]. A series of surface side reactions are triggered by nucleophilic attack and oxidation of solvents (primarily ethylene carbonate (EC)) [16,17], which produce H⁺/H₂O, hydrolyze LiPF₆, and form corrosive HF, leading to Co dissolution in return. Regarding oxygen evolution, the oxygen ions in the outermost layer are under-coordinated and more likely to be oxidized and released during delithiation [18]. The resulting oxygen vacancies can migrate inward, leading to bulk structural degradation. Additionally, the accumulation of solvent decomposition products and surface structural degradation caused by Co dissolution and oxygen release, impeding Li⁺ transport across the interphase [19]. Furthermore, particle cracking is associated with the

* Corresponding authors.

E-mail addresses: liut@anl.gov (T. Liu), xiajing@mail.ipc.ac.cn (J. Xia), wangchunyang@imr.ac.cn (C. Wang), panfeng@pkusz.edu.cn (F. Pan).

¹ These authors contributed equally.

reversibility of phase transition from O3 to H1-3 at 4.55 V [20], which is also significantly influenced by the oxygen evolution [21]. Therefore, the key to achieving high-voltage cycle stability in LCO is to prevent surface under-coordinated oxygen release and regulate the electrode-electrolyte interfacial chemistry.

Surface modification is one of the most widely used and effective strategies to enhance the electrochemical performance of high-voltage LCO [22]. Various types of coating materials, such as metal oxides [23], metal fluorides [24], solid electrolytes/other ionic conductors [25] and polymers [26] have been used to modify the interface for block the side reactions. In pursuit of an effective blocking effect, coupled with the uneven distribution of the coating materials, the coating thickness of the localized regions may exceed tens of nanometers, negatively affecting specific capacity and lithium-ion diffusion kinetics [27,28]. Furthermore, due to the distinct texture and weak chemical bond between the coating layer and the bulk phase, the coating layer may peel off thus undermining prolonged cycling stability. Therefore, to further enhance the lifespan of high-voltage LCO, an atomic-thin coating layer with multifunctional effects, including regulation of interfacial chemistry and stabilization of surface under-coordinated oxygen, is urgently needed.

In this work, a novel surface SO_4 tetrahedron modification strategy was developed. Specifically, surface-bonded SO_4 tetrahedrons, originating from under-coordinated surface oxygens and SO_2/O_2 gas, are introduced onto the surface of lithium cobalt oxide. The surface-bonded SO_4 tetrahedron not only suppresses oxygen evolution through a bonding effect but also mitigates side reactions between active material and electrolyte via an interface shielding effect. The interface shielding effect is related to the control of species (such as EC and PF_6^-) in the inner Helmholtz layer (IHL) by the SO_4 tetrahedron layer. The multifunctionality of the surface-bonded SO_4 tetrahedron was validated

through both first-principles calculations and experiments. When applied to Mg and Ce co-doped LCO (LCO-MC), this strategy significantly enhances its high-voltage electrochemical performance. LCO-MC+S retained 84 % of its capacity with an average Coulombic efficiency (ACE) of 99.94 % after 1000 cycles at 3.0–4.6 V and 1C, and 80 % capacity retention with an ACE of 99.68 % after 200 cycles at 3.0–4.7 V and 1C.

2. Results and discussion

The formation process of surface SO_4 tetrahedrons on the surface of LCO from SO_2 , O_2 and surface under-coordinated oxygen was theoretically simulated. For simplicity, we calculated the formation energy of a surface SO_4 tetrahedron based on SO_3 and surface under-coordinated oxygen of LCO, which was -2.509 eV, indicating that this process is thermodynamically favorable. The optimal connection is presented in Fig. S1, showing the surface SO_4 tetrahedron sharing one oxygen atom with LCO and forming two Co-O bonds with the under-coordinated cobalt atoms. EC is the most commonly used solvent in the commercial electrolytes of LIBs due to its multiple functions [29]. However, decomposition of EC on the cathode side by Co^{4+} and $\text{O}^{\alpha-2}$ at high voltages leads to cathode interfacial degradation (oxygen vacancy formation and low-valence oxide phase formation) and organic-rich CEI formation. Thus, we calculated the adsorption energies of EC on the (104) surfaces of LCO and surface SO_4 tetrahedron-bonded LCO (LCO+S) using density functional theory. As shown in Fig. 1a, the adsorption energy of EC on the surface of LCO and LCO+S was -0.952 eV and 0.586 eV, respectively. This result revealed that the adsorption of EC on LCO is energetically favorable, whereas the adsorption of EC on LCO+S is endothermic. The significantly reduced adsorption energy

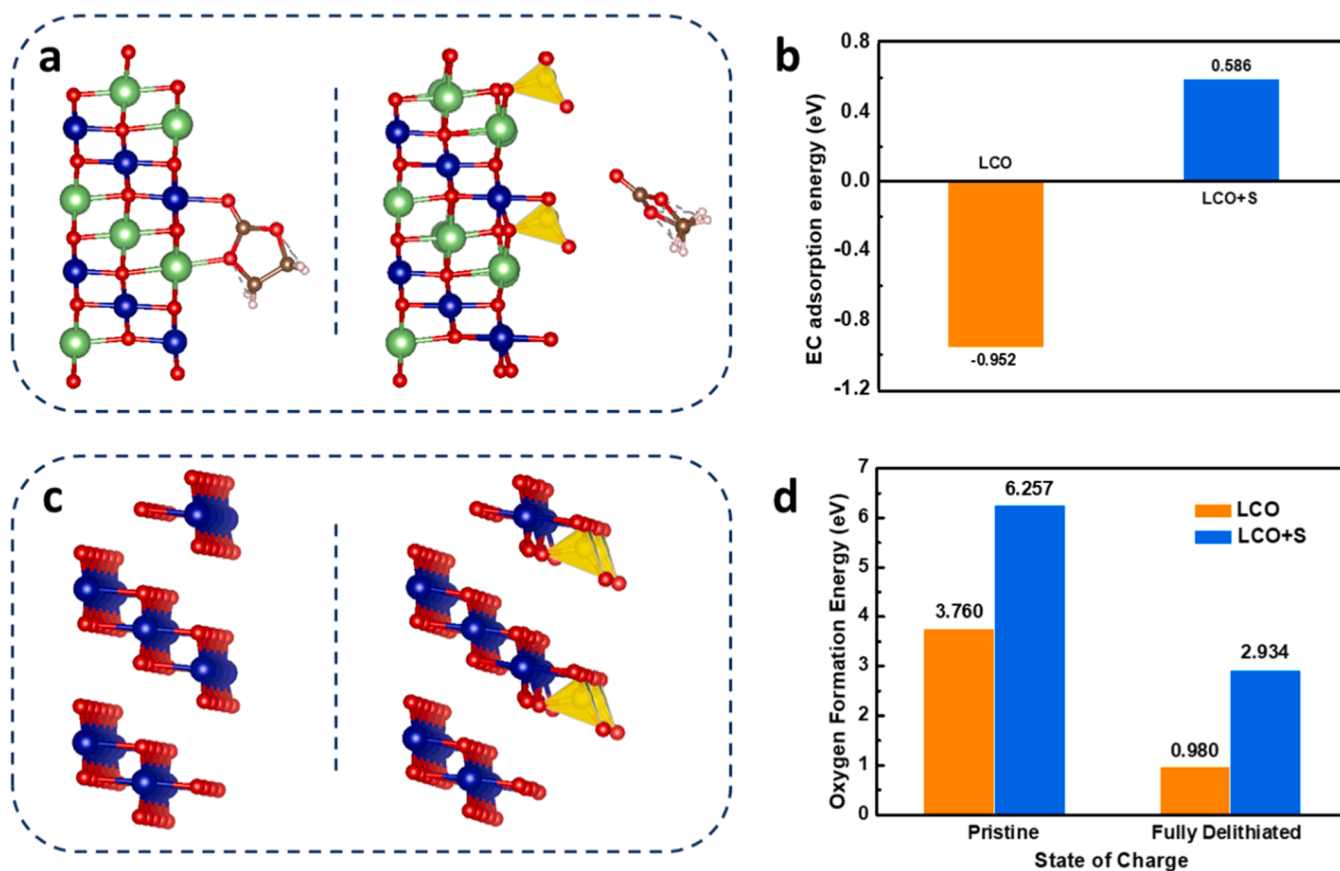


Fig. 1. The model used to calculate the adsorption energy between LCO/LCO+S and EC (a); the calculated adsorption energies between EC and LCO/LCO+S (b); the model of LCO/LCO+S in the delithiated states used for the calculation of oxygen vacancy formation energy (c); the calculated oxygen vacancy formation energies of LCO/LCO+S both in the pristine and delithiated states.

indicated lower adsorption capacity, thus significantly mitigating nucleophilic attack and oxidation [30]. In addition to this interaction, the oxygen vacancy formation energies on the surfaces of LCO and LCO+S in pristine and fully delithiated states were also calculated (Figs. 1b and S2). After surface SO_4 tetrahedron bonding, the oxygen vacancy formation energy increased to 2.934 eV for LCO+S, which is much higher than the 0.980 eV for LCO in the fully delithiated state, indicating that oxygen evolution is significantly hindered in LCO+S. Therefore, the SO_4 tetrahedron on the surface of LCO not only mitigates side reactions with the electrolyte (shielding effect) but also suppresses oxygen evolution into the solution (bonding effect), and its beneficial effects on LCO are schematically illustrated in Fig. S3. Further electrochemical tests demonstrated that the ACE and cycling stability of LCO+S were notably improved, verifying the reduction of side reactions at the cathode-electrolyte interface mediated by the surface SO_4 tetrahedrons (Fig. S4).

This strategy was also applied to LCO-MC to confirm the effects of surface SO_4 tetrahedrons further. SEM images of LCO, LCO+S, LCO-MC

and LCO-MC+S are displayed in Figs. 2a–c and S5a. The average particle size is approximately 5 μm for LCO and LCO+S and 3 μm for LCO-MC and LCO-MC+S, implying that Mg and Ce co-doping restricted grain growth to some extent. The Rietveld refined XRD data show that all samples are composed of a single phase of hexagonal R-3m structure (Figs. 2d–f and S5b). The refined results are listed in Table S1. In comparison with LCO (14.0477 Å), the increased lattice parameter c for LCO-MC (14.0509 Å) and LCO-MC+S (14.0510 Å) will enhance the lithium-ion transport kinetics [31], due to co-doping of the Mg and Ce into the lattice. The occupation ratio of heavy elements (Mg and Ce) at the Li site for LCO-MC and LCO-MC+S is 0.77 % and 0.49 %, respectively, directly proving the successful doping of the foreign ions at the Li sites. SEM-EDS mapping of LCO-MC+S shows the uniform distribution of Co, O, Mg, Ce and S elements (Fig. 2g). XPS etching result proves that the S with valence of +6 only presents on the surface of LCO-MC+S (Fig. S6a and b) [32]. As shown in Fig. S6c, the lattice oxygen peak of LCO-MC+S is 291.30 eV, which is higher than that of LCO (291.15 eV), implying that SO_4 tetrahedrons were bonded on the surface of LCO-MC+S, forming

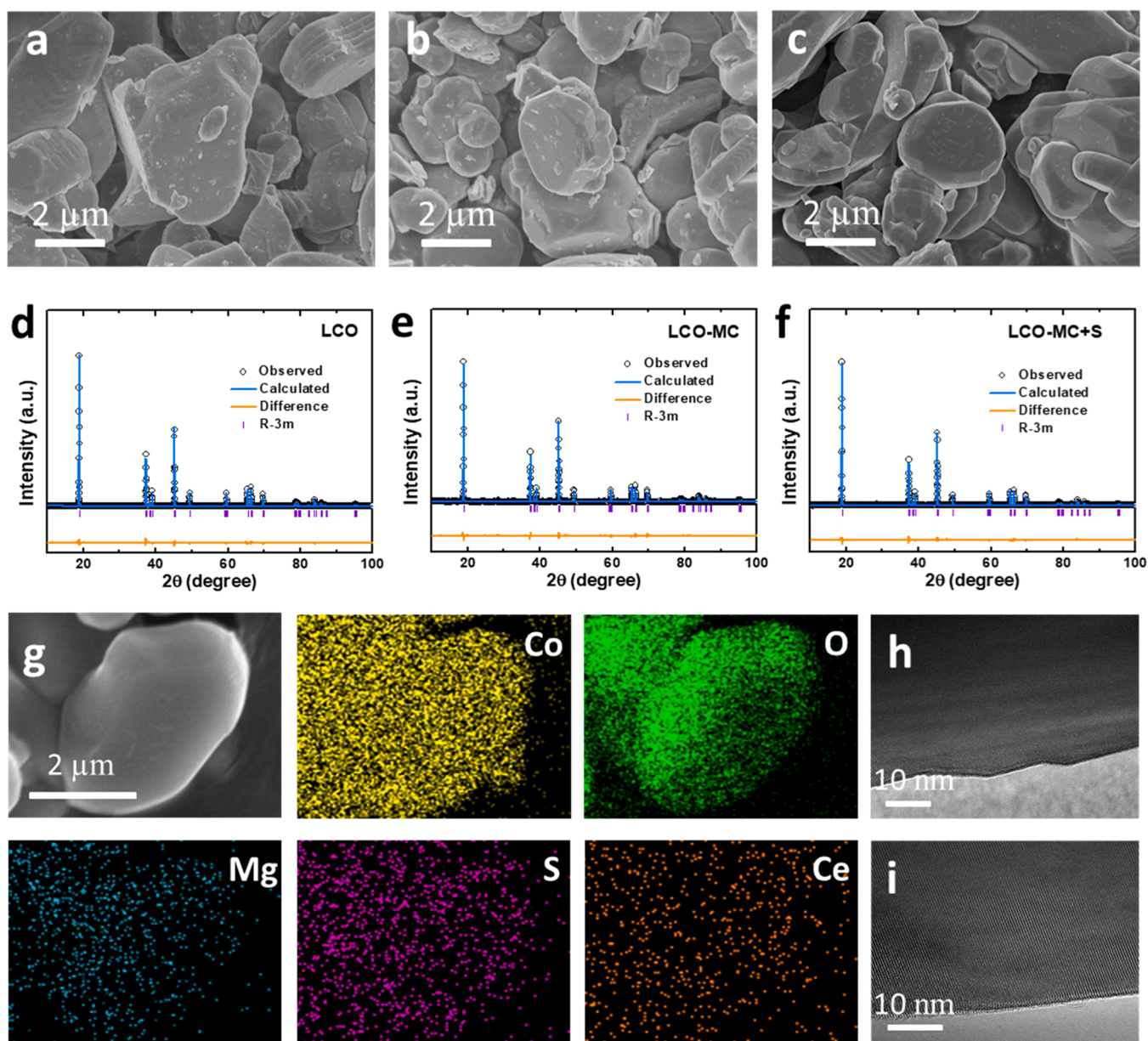


Fig. 2. SEM images of LCO (a), LCO-MC (b) and LCO-MC+S (c); refined XRD data of LCO (d), LCO-MC (e) and LCO-MC+S (f), respectively; SEM-EDS mapping of LCO-MC+S (g); HRTEM images of LCO(h) and LCO-MC+S (i).

metal-O-S bonds [33]. Additionally, both LCO and LCO-MC+S surface exhibit a layered structure, indicating that doping and surface SO_4 tetrahedron modification have negligible effects on the surface structure (Fig. 2h, i). There is no perceptible coating layer on the surface of LCO-MC+S, which indicates that the surface-bonded SO_4 tetrahedrons layer is quite thin, probably due to the self-limiting reaction between LCO and SO_2 .

To further evaluate the high-voltage performance of the samples, the cells were galvanostatic tested within a voltage range of 3.0–4.6 V. As shown in Fig. 3a, the samples exhibited a similar discharge capacity of 219 mAh g^{-1} at 0.1C ($1\text{C} = 280 \text{ mA g}^{-1}$), while the charge capacity was different. Thus, the initial Coulombic efficiency (ICE) for LCO, LCO-MC and LCO-MC+S was 95.2 %, 96.1 % and 97.8 %, respectively. LCO-MC and LCO-MC+S exhibited comparable rate performance (Fig. 3b), which was much better than that of LCO. This indicates that Mg and Ce doping can significantly enhance the lithium diffusion kinetics. Remarkably, LCO-MC+S exhibited a capacity retention of 84 % after 1000 cycles at 1C, while LCO and LCO-MC showed capacity retention of 18 % and 80 % after only 300 cycles (Fig. 3c). The corresponding Coulombic efficiency of the samples during cycling was also compared in Fig. 3d. LCO-MC+S exhibited an ACE of 99.92 % and 99.94 % after 300 and 1000 cycles, respectively. In contrast, the ACE of LCO and LCO-MC after 300 cycles was only 99.50 % and 99.80 %, respectively. Even though SO_2 gas treatment may raise cost for large-scale production due to safety concerns, the high-voltage cycling stability of LCO-MC+S is outstanding among Lithium cobalt oxides (Table S2). In addition, the minimum leakage current density of LCO-MC+S was $2.96 \mu\text{A cm}^{-2}$ (floating charge at 4.6 V and 45°C), much lower than $8.94 \mu\text{A cm}^{-2}$ for LCO (Fig. S7a). Even after floating charge for 90 h, the leakage current density of LCO-MC+S only increased to $5.46 \mu\text{A cm}^{-2}$, which was significantly lower than $33.23 \mu\text{A cm}^{-2}$ for LCO (Fig. S7b). The exceptional ACE and suppressed leakage current density of LCO-MC+S indicate negligible side reactions between the active materials and electrolyte, even at 4.6 V. Additionally, as shown in Fig. S8, the voltage decay was significantly suppressed during cycling in LCO-MC+S compare to the other three counterparts. Additionally, when cycled at 3.0–4.7 V and 1C, LCO-MC+S exhibits a capacity retention of 80 % (corresponding to a maximum value of 220 mAh g^{-1}) and an ACE of 99.68 % after 200 cycles (Fig. 3e–f), as well as 62 % capacity retention after 500 cycles (Fig. S9a). In addition to surface modification, structure engineering to eliminate layer glide and O1 phase formation is concurrently necessary for further enhancing the stability at 4.7 V. The cyclic voltammetry (CV) profiles of the samples, presented in Fig. S10, showed that the reduction peak intensity for LCO decreased gradually with the increase in cycle count, while that for LCO-MC+S increased gradually. This seemingly contradictory result indicates that the reversibility of LCO is poor and there is an activation process for LCO-MC+S.

In-situ XRD measurements were conducted to investigate the phase evolution and volume variation during the charge/discharge process (Figs. 4 and S11). Changes in the (003) and (110) peaks are related to the variation of lattice parameter c and a , respectively. The anisotropic volume variation in LCO, as reported in our recent works [20], can cause serious interphase stress. The slab glide during the phase change from O3 to H1-3 is schematically illustrated in Fig. 4a and b, with a gliding vector of $(2/3, 1/3, 0)$. Thus, the Co-O slab glide will cause (101), (104) and (107) peaks to abruptly shift to lower angles, while the (012), (015) and (018) peaks shift to higher angles [6]. As shown in Figs. 4c,d and S11, the (003) peak shift of LCO-MC+S and LCO-MC was 1.19° , which was slightly lower than the 1.21° shift for LCO. The O1a (in H1-3) phase was slightly intense in LCO relative to LCO-MC+S or LCO-MC, implying that Mg and Ce co-doping shows a limited effect to the H1-3 phase transformation. This result indicates that Mg&Ce doping and SO_4 tetrahedron modification improve phase transition reversibility rather than inhibit phase transition.

The atomic scale surface structure of the cycled samples was investigated by high-angle annular dark-field scanning transmission electron

microscope (HAADF-STEM). As shown in Fig. 5a, a cation-densified layer ($\sim 8 \text{ nm}$), including rock-salt and spinel phases, was formed at the surface of LCO. Additionally, as confirmed by the low-magnification image (Fig. 5b), this cation-densified layer is uniformly formed on the surface. The complete coverage of the cation-densified layer blocks the transport of Li^+ ions and thus reduces the capacity [34]. In contrast, the LCO-MC+S maintained its original layered structure after enduring the same operational conditions (Fig. 5c). Moreover, no cation-densified layer was observed on the surface of LCO-MC+S (Fig. 5d). Further, the surface structure of the three samples after 300 cycles were investigated by TEM. Glide (Fig. S12b) and pores (Fig. S12c) were observed in the 300-cycled LCO. The formation of pores indicates oxygen evolution and Co dissolution. In addition, the surface layered structure was completely transformed into a spinel structure (Fig. S12c,d) or a spinel and rock-salt mixed structure (Fig. S12 f, g,i–k). For 300-cycled LCO-MC, cracks and glide were also formed (Fig. S13a,c,d), and the surface layered structure was also transformed into a spinel structure completely (Fig. S13b–f). The transformation of layered LCO into spinel Co_3O_4 or rock-salt (CoO) is accompanied by lattice oxygen evolution because the O/Co ratio of the generated structures is lower than that of the layered LCO. In contrast, no glide/crack or pores were observed, and only a small part of the layered structure was transformed into a spinel structure on the 300-cycled LCO-MC+S surface (Fig. S14). These results indicate that the surface-bonded SO_4 tetrahedrons can significantly mitigate the surface degradation of the sample.

To further investigate the surface degradation of the samples, time-of-flight secondary ion mass spectrometry (TOF-SIMS) was performed to characterize the spatial distribution of fragments after 100 cycles at 4.6 V. The 3D images of Li-, Co-, O- and LiF2- fragments for the LCO and LCO-MC+S are displayed in Fig. 6a and b. The Co- and Li- fragments are well overlapped for cycled LCO-MC+S, while the Li- fragment is less pronounced in the surface region compared to the Co- fragment for cycled LCO. This is further confirmed by the depth profiles and their intensity ratio (Fig. 6c–e). As shown in Fig. S15, this near-surface Lithium-barren phenomenon was also observed in the cycled LCO-MC. A lower Li signal in the surface region indicates the formation of Co_3O_4 or CoO phases in cycled LCO due to surface degradation, which coincides with the TEM results. As shown in Fig. S16, the Li SO_4 - fragments are covered on the Co- fragments well, implying the SO_4 tetrahedrons layer didn't degrade over time and protects the cathode persistently. Additionally, the intensity of LiF2- for cycled LCO-MC+S was higher than that of LCO, implying that there is more LiF on the surface of cycled LCO-MC+S, consistent with the XPS results in Fig. S17. Furthermore, the content of surface O on the surface of cycled LCO is higher than that of cycled LCO-MC+S (Fig. S17) [35], indicating that the solvent (such as EC) decomposition was effectively mitigated on the surface of LCO-MC+S. The high content of inorganic LiF ensures the high chemical stability of the surface layer at high voltages, which is crucial for the high-voltage stability of LCO [36].

The polarization and Li^+ apparent diffusion coefficient (D_{Li^+}) of the samples after long-term cycling (100 cycles at 4.6 V and 1C) were revealed by the galvanostatic intermittent titration technique (GITT). Fig. S18 shows the GITT curves of the three samples tested at a current density of 28 mA g^{-1} . The average overpotential of LCO during the charge process is 0.0837 V, which is about an order of magnitude higher than 0.0084 V for LCO-MC+S. Moreover, the overpotential difference is more pronounced during the discharge process (Fig. S18a). The D_{Li^+} of LCO, LCO-MC and LCO-MC+S is displayed in Fig. S18b–d, respectively. Most importantly, the average D_{Li^+} of LCO-MC+S is $3.51 \times 10^{-11} \text{ cm}^2 \text{ s}^{-1}$, which is higher than $1.84 \times 10^{-11} \text{ cm}^2 \text{ s}^{-1}$ and $2.06 \times 10^{-12} \text{ cm}^2 \text{ s}^{-1}$ for LCO-MC and LCO, respectively.

In-situ galvanostatic electrochemical impedance spectra (GEIS) measurement was conducted to monitor the dynamic and CEI evolutions. The time-voltage profiles of the LCO and LCO-MC+S for GEIS testing are presented in Fig. S19a. The variation of Nyquist plots during the charging/discharging process for 200-cycled LCO and 200-cycled

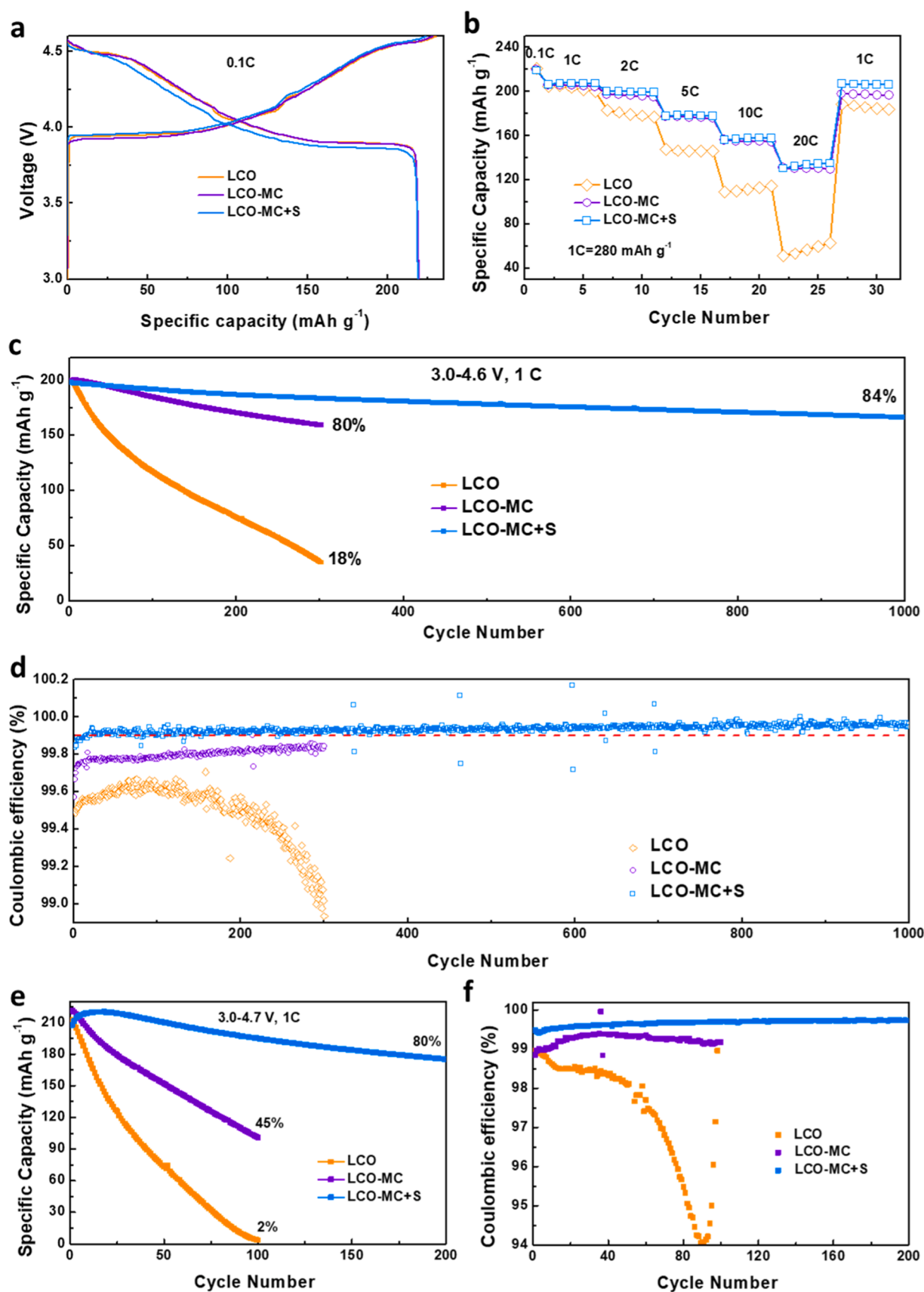


Fig. 3. Electrochemical performance comparison of LCO, LCO-MC and LCO-MC+S. Charge-discharge profiles (a) and rate performance (b) of the samples; cycling performance (c) and the corresponding Coulombic efficiency of the samples at 3.0–4.6 V (d); cycling performance (e) and the corresponding Coulombic efficiency (f) of the samples at 3.0–4.7 V.

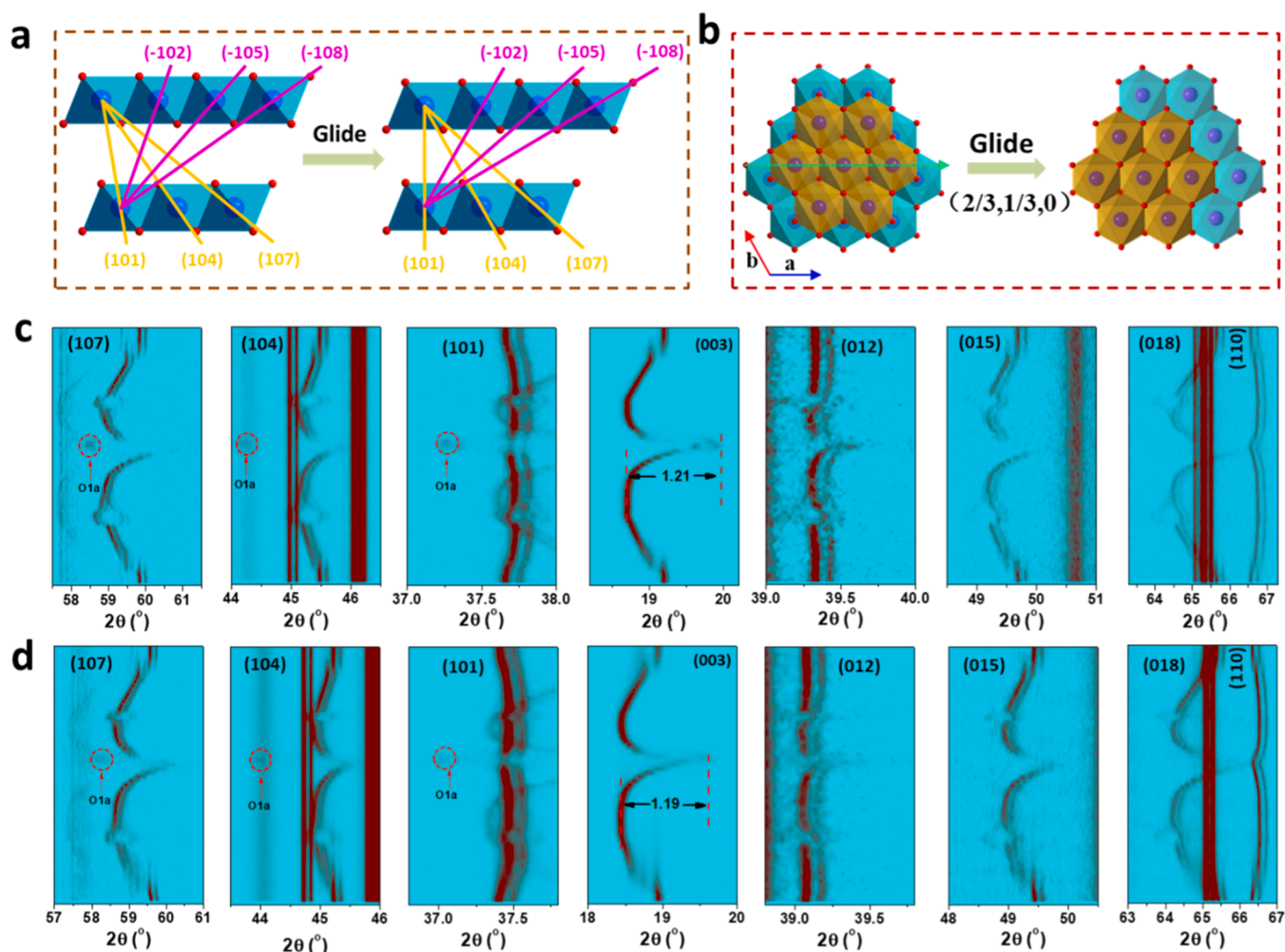


Fig. 4. Schematic illustration of the gliding process during phase transformation from O3 to O1a, shown from the side (a) and top (b) perspectives. *In-situ* XRD peak evolution of LCO (c) and LCO-MC+S (d) during the first cycle. The green dotted arrow in (b) indicates the side-view orientation of (a).

LCO-MC+S is illustrated in Fig. S19b and S19c, respectively. Each Nyquist plot exhibits two semicircles, which could be attributed to solid electrolyte interface resistance (R_{sei}) and charge transfer resistance (R_{ct}), respectively [19]. For better comparison, the curves were fitted with an equivalent circuit model (Fig. S19b inset). LCO and LCO-MC+S exhibit a R_{ct} of 1525.0 and 269.4 Ω , respectively, at 4.6 V. LCO showed much higher R_{ct} with greater variation throughout the process (Fig. S19d). In detail, during charging, R_{ct} for LCO decreases significantly in the voltage range of 3.88–4.20 V, remains relative steady in the voltage range of 4.20–4.50 V, and increases dramatically from 4.50 V to 4.60 V. During discharging, R_{ct} shows similar variations across the three voltage ranges. The dramatic variation of R_{ct} in LCO during different SOC is indicative of significant dynamic CEI evolution [37,38]. These results indicate that the CEI for LCO-MC+S is more stable than that of LCO. To further interpret the EIS, distribution of relaxation time (DRT) [39] analysis was conducted. In the time-domain-based DRT pattern, the peak positions and areas represent the relaxation time and impedance of the specific electrochemical process, respectively. The results, in Fig. S19e–i, revealed that the charge transfer in LCO-MC+S cell (0.54 s) is more rapid than in LCO (3.1 s).

Thermal instability is a major safety concern in the application of LCO batteries at high voltages. We investigated the thermal stability of the fully-charged cathodes by simultaneously probing gas evolution and weight change during abuse heating. As shown in Fig. S20a, the onset temperature of decomposition was enhanced, and the total mass loss was reduced for LCO-MC+S compare to LCO. Specifically, the onset

temperature of decomposition was 207 °C for LCO and 230 °C for LCO-MC+S. Correspondingly, a sharp O_2 evolution peak at 274 °C for LCO and a broad O_2 evolution peak at 310 °C for LCO-MC+S were observed (Fig. S20b). Additionally, the CO_2 evolution peak shifted to a higher temperature for LCO-MC+S relative to LCO (Fig. S20c). These results clearly reveal that the thermal stability of LCO-MC+S is improved.

3. Conclusion

We developed a novel surface SO_4 tetrahedron modification strategy to improve the performance of lithium cobalt oxide at high voltages. Specifically, we constructed surface-bonded SO_4 tetrahedrons by treating the LCO surface with SO_2 gas. Theoretical calculations and experimental results revealed that SO_2 reacts spontaneously with under-coordinated oxygen atoms on the LCO surface, forming surface-bonded SO_4 tetrahedrons. Based on our calculations, the constructed surface SO_4 tetrahedrons significantly affect the surface properties by tuning the adsorption energies of EC, influencing the species in the inner Helmholtz layer (shielding effect), and increasing the surface oxygen vacancy formation energy (bonding effect). These effects of surface modification were verified through a series of experiments, including analysis of the CEI composition and thickness, surface structure evolution, *in-situ* EIS evolution, and leakage current density. When this surface modification strategy was applied to Mg&Ce co-doped LCO, the cycling performance and average Coulombic efficiency at high voltages were further significantly enhanced. Upon testing at 3.0–4.6 V and 1C,

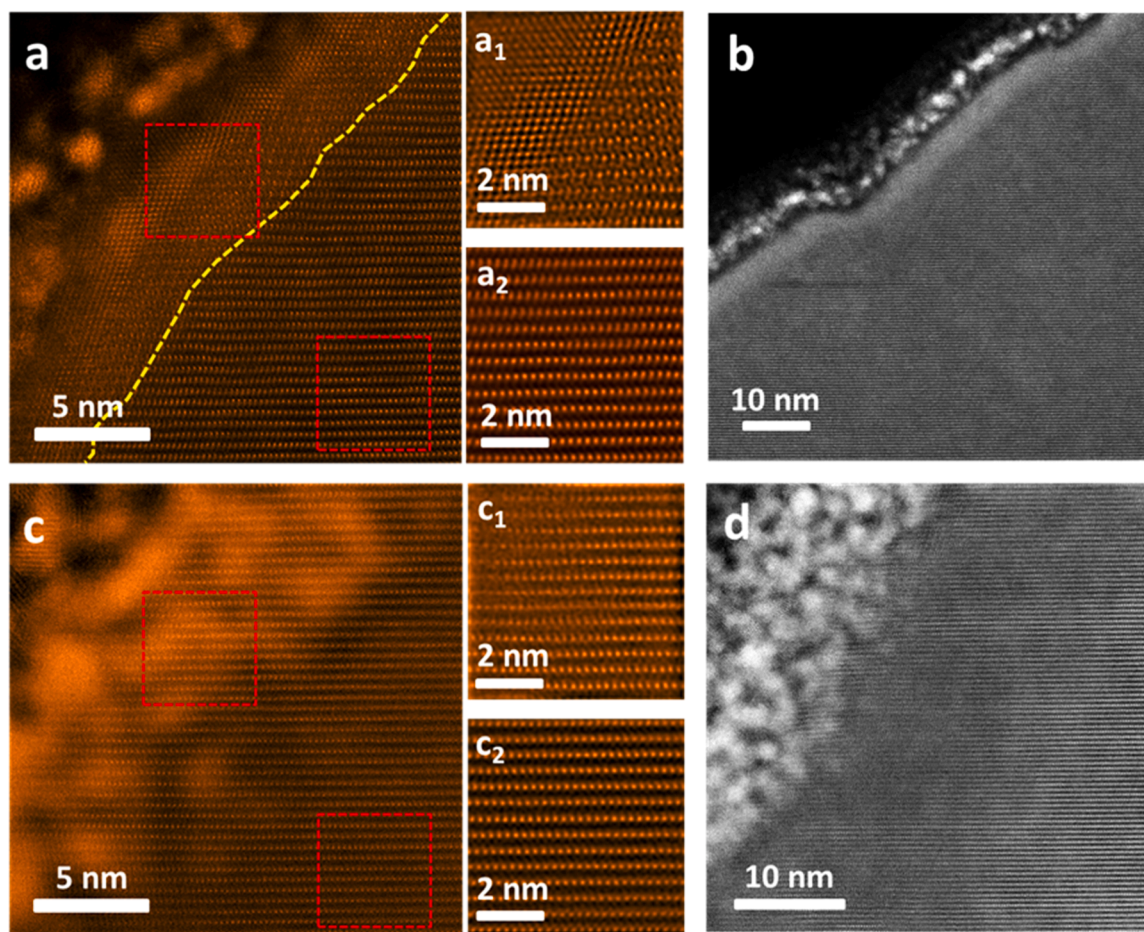


Fig. 5. HAADF-STEM images of LCO (a,b) and LCO-MC+S (c,d) after 100 cycles at 4.6 V. (a₁) and (a₂) are the enlargements of the square regions in image (a); (c₁) and (c₂) are the enlargements of the square regions in image (c).

LCO-MC+S demonstrated a capacity retention of 84 % after 1000 cycles, compared to 18 % and 80 % retention for LCO and LCO-MC after only 300 cycles. Furthermore, LCO-MC+S exhibited a capacity retention of 80 % after 200 cycles at 3.0–4.7 V and 1C, compared to 2 % and 45 % retention for LCO and LCO-MC after only 100 cycles. This work introduces a novel approach to designing high-voltage cathodes, opening up new possibilities for high-energy lithium-ion batteries.

4. Experimental section

Materials synthesis: the bare LiCoO₂ and Mg, Ce co-doped LiCoO₂ were prepared using a solid-state reaction method. Li₂CO₃ (98 %), Co₃O₄ (99.9 %), MgO (99 %) and CeO₂ (99.9 %) were used as the raw materials. The Li:Co molar ratio was 1.05:1 in the precursor of LiCoO₂, while the molar ratio of Li, Co, Mg and Ce was 1.035:0.9975:0.0075:0.0025 in the precursor of Mg, Ce co-doped LiCoO₂. The raw materials were ground in an agate mortar for half-hour to form the mixed precursor, which was calcined at 550 °C for 4 h, followed by 950 °C for 10 h in air, to obtain the products. To obtain the final products, the as-prepared lithium cobalt oxides were mixed with sulfur (S) powders (molar ratio of LiCoO₂ to S = 1:0.05) and sintered for a second time at 550 °C for 2 h, followed by 850 °C for 4 h in air.

Structural and morphological characterizations: The crystal structure of the samples was analyzed via X-ray diffraction (XRD) using a Bruker D8 Advance diffractometer (Cu K α radiation, $\lambda=0.154$ nm). *In-situ* XRD data were collected using the same instrument with the *in-situ* cell accessory (approximately 6 min to collect each pattern). Rietveld

refinements of XRD patterns were performed using FullProf software. Scanning electron microscopy (SEM, Zeiss SUPRA-55), equipped with an X-Max EDS detector, was used for morphological and elemental distribution characterization. High-resolution field-emission transmission electron microscopy (FETEM, JEOL-3200FS, 300 kV) was employed for local structural investigation. The atomic structures of the samples were investigated via high-angle annular dark-field scanning transmission electron microscopy (HAADF-STEM, JEM-ARM300F, Japan). The cross-sectional sample of the individual particle was prepared using a focused ion beam (FIB/SEM, Nova200 NanoLab, Thermo Fischer Scientific, USA). The chemical states of the elements were analyzed using X-ray photoelectron spectrometry (XPS) on an ESCALab 250Xi electron spectrometer (Thermo Fisher Scientific, USA). Simultaneous thermal analyzer coupled with gas chromatography-mass spectrometry (STG-GC/MS, STA8000-Frontier-Clarus SQ8, PerkinElmer, Netherlands) was employed to detect gas evolution and weight loss simultaneously of the charged electrode during heating (4.6 V; LCO: PVDF: acetylene black = 94: 3: 3; 30–600 °C). The surface properties of the cycled cathodes were obtained using time-of-flight secondary ion spectrometry (TOF-SIMS, 5 iontof, PHI NanoTOFII, Germany).

Electrochemical measurements: the active material (80 %), polyvinylidene fluoride (PVDF, 10 wt %) and acetylene black (10 wt %) were thoroughly mixed in N-methyl-2-pyrrolidone (NMP) solvent to form a slurry. The slurry was cast onto aluminum foil and dried at 105 °C in a vacuum oven overnight to form the electrodes. Electrochemical performance was evaluated in CR2032 coin cells, with Celgard 2316 as the separators, lithium metal sheets as anodes, and an electrolyte of 1 M LiPF₆ in a 1:1 vol ratio of ethylene carbonate (EC) to dimethyl carbonate

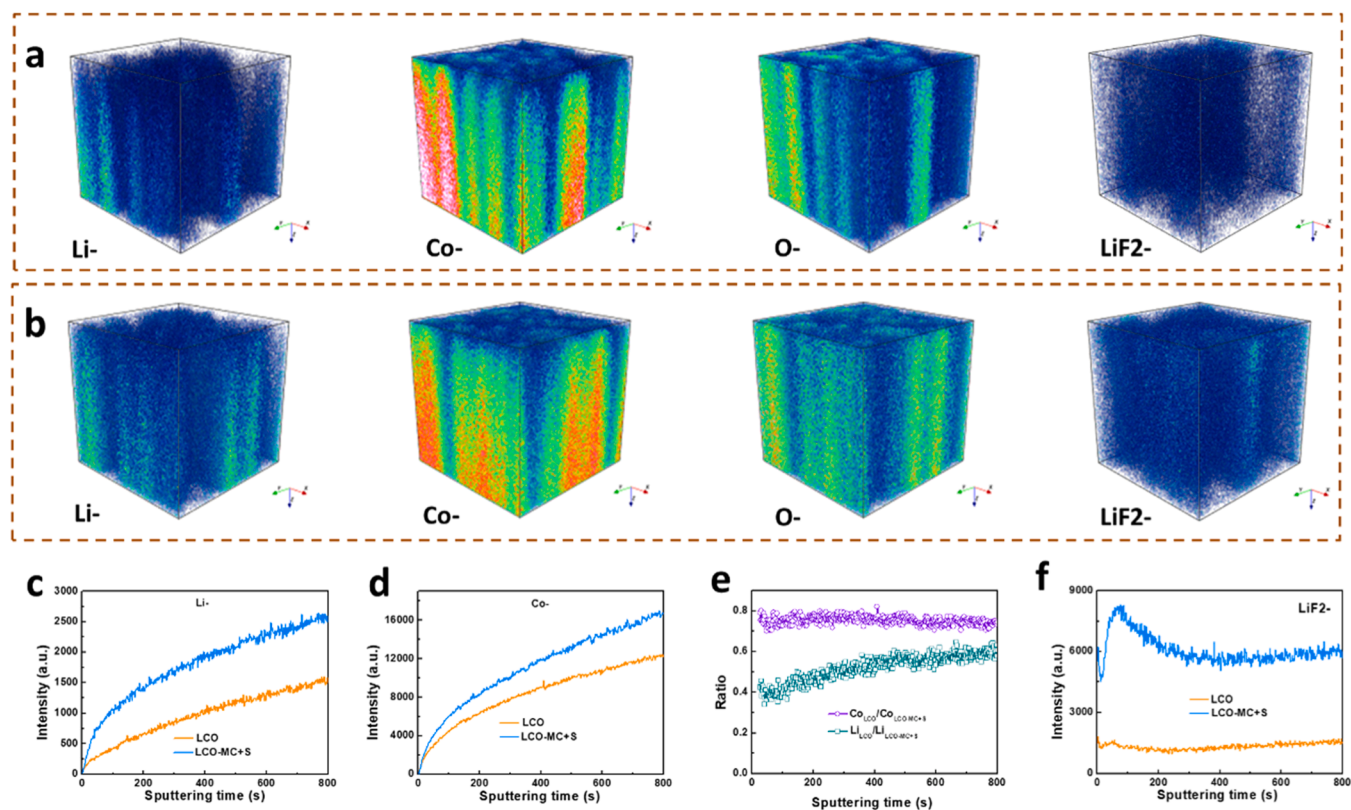


Fig. 6. TOF-SIMS results of the electrodes after 100 cycles. The 3D reconstruction of Li-, Co-, O- and LiF2- fragments on the surface of LCO (a) and LCO-MC+S (b); comparison of the depth profiling of Li- (c), Co- (d) and LiF2- (f) fragment; the Li- and Co- ratio evolution in the two samples during sputtering (e).

(DMC) with a 5 % fluoroethylene carbonate (FEC) additive. The cells were galvanostatically tested at 3.0–4.6/4.7 V ($1C = 280 \text{ mA g}^{-1}$). Cyclic voltammetry (CV) and *in-situ* electrochemical impedance spectroscopy (EIS) measurements were performed on a Solartron workstation. The galvanostatic intermittent titration technique (GITT) and Floating charge tests were conducted using a Neware battery test system (CT-4008T-5V10mA-164, Shenzhen, China).

Calculations details: All calculations were carried out utilizing the plane-wave-based density functional theory (DFT), implemented within the Vienna ab initio simulation package (VASP) [40–42]. The Perdew–Burke–Ernzerhof (PBE) formulation of generalized gradient approximation (GGA), grounded in the projector-augmented wave (PAW) method, was employed to describe the exchange-correlation potential for electrons [43–45]. The cutoff energy was set at 520 eV, and the electronic energy convergence was set to 10^{-5} eV. For surface slab calculations, the bottom atomic layer was constrained to the optimized bulk structure, while the upper two layers were allowed to relax. A vacuum of 20 Å was introduced along the z-axis, perpendicular to the terminating (104) surface, to prevent spurious interactions between periodic images of the surface slabs. The Brillouin zone sampling for surface slab calculations used Monkhorst–Pack k-point meshes, with a grid density of $2 \times 2 \times 1$. To adequately describe the localization of transition-metal d-electrons, the GGA+*U* method was adopted, incorporating strong correlation interactions [46,47]. The *U* parameter for cobalt was set to 3.3 eV [48]. Atomic geometries were optimized until the forces acting on the atoms were below 0.02 eV Å^{-1} , and spin polarization was considered. Additionally, the DFT-D3 semi-empirical van der Waals correction was employed to account for dispersion forces during the structure relaxation [49].

The adsorption energy (E_{ads}) was calculated using the expression: $E_{\text{ads}} = E_{\text{slab+EC}} - E_{\text{slab}} - E_{\text{EC}}$, where $E_{\text{slab+EC}}$ represents the energy of the slab with the adsorbed solvent molecule, E_{slab} is the energy of the clean slab, and E_{EC} is the energy of the isolated solvent molecule.

To assess the thermodynamic stability of oxygen on the model surface, the oxygen vacancy formation energy $E_f(V_O)$ was calculated using the equation: $E_f(V_O) = E(V_O) + 1/2 E(O_2) - E(\text{pristine})$, where $E(V_O)$ and $E(\text{pristine})$ correspond to the total energies of the oxygen-deficient and pristine structure, respectively, and $E(O_2)$ refers to the energy of the oxygen molecule. A correction of -1.36 eV was applied to the O_2 molecule energy in all calculations to address self-interaction errors within DFT [48].

CRediT authorship contribution statement

Xinghua Tan: Writing – original draft, Methodology, Investigation, Funding acquisition, Formal analysis, Conceptualization. **Zhongxing Xu:** Resources, Investigation, Formal analysis. **Zhefeng Chen:** Visualization, Software, Methodology. **Yutao Niu:** Software, Methodology. **Haoyu Xue:** Formal analysis. **Xinghan Chen:** Visualization. **Shenyang Xu:** Resources. **Yongzhi Liang:** Data curation. **Xulin Mu:** Investigation. **Shunning Li:** Software. **Tongchao Liu:** Writing – review & editing, Project administration. **Jing Xia:** Writing – review & editing, Project administration, Investigation. **Chunyang Wang:** Writing – review & editing, Supervision, Funding acquisition. **Feng Pan:** Writing – review & editing, Supervision, Project administration, Funding acquisition.

Declaration of competing interest

The authors declare no conflict of interest.

Acknowledgments

X.T., Z.X. and Z.C. contributed equally to this work. This work was financially supported by the Basic and Applied Basic Research Foundation of Guangdong Province (No.2023A1F515111131), the National Natural Science Foundation of China (No. 92472206), the Major Science

and Technology Infrastructure Project of Material Genome Big-science Facilities Platform supported by Municipal Development and Reform Commission of Shenzhen, International Joint Research Center for Electric Vehicle Power Battery and Materials (No.2015B01015), Guangdong Key Laboratory of Design and Calculation of New Energy Materials (No. 2017B030301013), Shenzhen Key Laboratory of New Energy Resources Genome Preparation and Testing (No. ZDSYS201707281026184), and Liaoning Provincial Science Fund for Distinguished Young Scholar (No. 2024JH3/50100017).

Supplementary materials

Supplementary material associated with this article can be found, in the online version, at [doi:10.1016/j.ensm.2025.104376](https://doi.org/10.1016/j.ensm.2025.104376).

Data availability

Data will be made available on request.

References

- R. Zhang, C. Wang, P. Zou, R. Lin, L. Ma, L. Yin, T. Li, W. Xu, H. Jia, Q. Li, S. Sainio, K. Kisslinger, S.E. Trask, S.N. Ehrlich, Y. Yang, A.M. Kiss, M. Ge, B.J. Polzin, S. J. Lee, W. Xu, Y. Ren, H.L. Xin, Compositionally complex doping for zero-strain zero-cobalt layered cathodes, *Nature* 610 (7930) (2022) 67–73.
- W. Huang, T. Liu, L. Yu, J. Wang, T. Zhou, J. Liu, T. Li, R. Amine, X. Xiao, M. Ge, L. Ma, S.N. Ehrlich, M.V. Holt, J. Wen, K. Amine, Unrecoverable lattice rotation governs structural degradation of single-crystalline cathodes, *Science* 384 (6698) (2024) 912–919 (1979).
- L. Qian, T. Or, Y. Zheng, M. Li, D. Karim, A. Cui, M. Ahmed, H.W. Park, Z. Zhang, Y. Deng, A. Yu, Z. Chen, K. Amine, Critical operation strategies toward high-performance lithium metal batteries, *Renewables* 1 (2) (2023) 114–141.
- Y. Liang, X. Zhu, X. Fan, D. Li, F. Xu, H. Yu, L.-Z. Fan, Surface-enriched Co engineering promoting electronic conductivity for single-crystalline Ni-based layered oxide cathodes, *Chem. Eng. J.* 485 (2024) 149575.
- J. Liu, J. Wang, Y. Ni, J. Liu, Y. Zhang, Y. Lu, Z. Yan, K. Zhang, Q. Zhao, F. Cheng, J. Chen, Tuning interphase chemistry to stabilize high-voltage LiCoO₂ cathode material via spinel coating, *Angew. Chem. Int. Ed.* 61 (35) (2022) e202207000.
- X. Tan, Y. Zhang, S. Xu, P. Yang, T. Liu, D. Mao, J. Qiu, Z. Chen, Z. Lu, F. Pan, W. Chu, High-entropy surface complex stabilized LiCoO₂ cathode, *Adv. Energy Mater.* 13 (24) (2023) 2300147.
- J.-N. Zhang, Q. Li, C. Ouyang, X. Yu, M. Ge, X. Huang, E. Hu, C. Ma, S. Li, R. Xiao, W. Yang, Y. Chu, Y. Liu, H. Yu, X.-Q. Yang, X. Huang, L. Chen, H. Li, Trace doping of multiple elements enables stable battery cycling of LiCoO₂ at 4.6 V, *Nat. Energy* 4 (7) (2019) 594–603.
- R. Konar, S. Maiti, N. Shpigel, D. Aurbach, Reviewing failure mechanisms and modification strategies in stabilizing high-voltage LiCoO₂ cathodes beyond 4.55V, *Energy Storage Mater.* 63 (2023) 103001.
- L. Wang, B. Chen, J. Ma, G. Cui, L. Chen, Reviving lithium cobalt oxide-based lithium secondary batteries-toward a higher energy density, *Chem. Soc. Rev.* 47 (17) (2018) 6505–6602.
- Q. Wang, N. Bai, Y. Xin, X. Fan, D. Zhang, Z. Li, Q. Sun, H. Sun, B. Wang, G. Wang, L.-Z. Fan, Synergistic effect of sulfolane-based composite polymer electrolyte and vinylidene carbonate/lithium difluoro(oxalato)borate interface modification on LiCoO₂ cathode, *J. Colloid Interface Sci.* 687 (2025) 552–560.
- W. Ding, H. Ren, Z. Li, M. Shang, Y. Song, W. Zhao, L. Chang, T. Pang, S. Xu, H. Yi, L. Zhou, H. Lin, Q. Zhao, F. Pan, Tuning surface rock-salt layer as effective O capture for enhanced structure durability of LiCoO₂ at 4.65 V, *Adv. Energy Mater.* 14 (13) (2024) 2303926.
- Z. Zhu, H. Wang, Y. Li, R. Gao, X. Xiao, Q. Yu, C. Wang, I. Waluyo, J. Ding, A. Hunt, J. Li, A surface Se-substituted LiCoO₂-_δSe_δ cathode with ultrastable high-voltage cycling in pouch full-cells, *Adv. Mater.* 32 (50) (2020) e2005182.
- Y. Zhang, Y. Katayama, R. Tataru, L. Giordano, Y. Yu, D. Fraggadakis, J.G. Sun, F. Maglia, R. Jung, M.Z. Bazant, Y. Shao-Horn, Revealing electrolyte oxidation via carbonate dehydrogenation on Ni-based oxides in Li-ion batteries by *in situ* Fourier transform infrared spectroscopy, *Energy Environ. Sci.* 13 (1) (2020) 183–199.
- Y. Yan, S. Weng, A. Fu, H. Zhang, J. Chen, Q. Zheng, B. Zhang, S. Zhou, H. Yan, C.-W. Wang, Y. Tang, H. Luo, B.-W. Mao, J. Zheng, X. Wang, Y. Qiao, Y. Yang, S.-G. Sun, Tailoring electrolyte dehydrogenation with trace additives: stabilizing the LiCoO₂ cathode beyond 4.6 V, *ACS Energy Lett.* 7 (8) (2022) 2677–2684.
- B.L.D. Rinkel, D.S. Hall, I. Temprano, C.P. Grey, Electrolyte oxidation pathways in lithium-ion batteries, *J. Am. Chem. Soc.* 142 (35) (2020) 15058–15074.
- L. Yu, H. Liu, Y. Wang, N. Kuwata, M. Osawa, J. Kawamura, S. Ye, Preferential adsorption of solvents on the cathode surface of lithium ion batteries, *Angew. Chem. Int. Ed.* 52 (22) (2013) 5753–5756.
- Z. Zhu, D. Yu, Z. Shi, R. Gao, X. Xiao, I. Waluyo, M. Ge, Y. Dong, W. Xue, G. Xu, W.-K. Lee, A. Hunt, J. Li, Gradient-morph LiCoO₂ single crystals with stabilized energy density above 3400 Wh L⁻¹, *Energy Environ. Sci.* 13 (6) (2020) 1865–1878.
- Q. Chen, Y. Pei, H. Chen, Y. Song, L. Zhen, C.Y. Xu, P. Xiao, G. Henkelman, Highly reversible oxygen redox in layered compounds enabled by surface polyanions, *Nat. Commun.* 11 (1) (2020) 3411.
- X. Tan, T. Zhao, L. Song, D. Mao, Y. Zhang, Z. Fan, H. Wang, W. Chu, Simultaneous near-surface trace doping and surface modifications by gas-solid reactions during one-pot synthesis enable stable high-voltage performance of LiCoO₂, *Adv. Energy Mater.* 12 (30) (2022).
- C. Lin, J. Li, Z.-W. Yin, W. Huang, Q. Zhao, Q. Weng, Q. Liu, J. Sun, G. Chen, F. Pan, Structural understanding for high-voltage stabilization of lithium cobalt oxide, *Adv. Mater.* 36 (6) (2024) 2307404.
- F. Guo, Y. Chen, Y. Song, Y. Deng, W. Hua, W. Yang, T. Chen, Z. Wu, L. Qiu, X. Guo, Oxygen vacancies driven by Co in the deeply charged state inducing intragranular cracking of Ni-rich cathodes, *Small* 20 (22) (2024) e2310321.
- S. Kalluri, M. Yoon, M. Jo, S. Park, S. Myeong, J. Kim, S.X. Dou, Z. Guo, J. Cho, Surface engineering strategies of layered LiCoO₂ cathode material to realize high-energy and high-voltage Li-ion cells, *Adv. Energy Mater.* 7 (1) (2017) 1601507.
- A. Zhou, Q. Liu, Y. Wang, W. Wang, X. Yao, W. Hu, L. Zhang, X. Yu, J. Li, H. Li, Al₂O₃ surface coating on LiCoO₂ through a facile and scalable wet-chemical method towards high-energy cathode materials withstanding high cutoff voltages, *J. Mater. Chem. A* 5 (46) (2017) 24361–24370.
- J. Qian, L. Liu, J. Yang, S. Li, X. Wang, H.L. Zhuang, Y. Lu, Electrochemical surface passivation of LiCoO₂ particles at ultrahigh voltage and its applications in lithium-based batteries, *Nat. Commun.* 9 (1) (2018) 4918.
- X. Qi, G. Wu, M. Wu, D. Li, C. Wang, L. Gao, S. Zhang, L.-Z. Fan, Deciphering and overcoming the high-voltage limitations of halide and sulfide-based all-solid-state lithium batteries, *J. Energy Chem.* 103 (2025) 926–935.
- X. Yang, L. Shen, B. Wu, Z. Zuo, D. Mu, B. Wu, H. Zhou, Improvement of the cycling performance of LiCoO₂ with assistance of cross-linked PAN for lithium ion batteries, *J. Alloy. Compd.* 639 (2015) 458–464.
- L. Zou, J. Li, Z. Liu, G. Wang, A. Manthiram, C. Wang, Lattice doping regulated interfacial reactions in cathode for enhanced cycling stability, *Nat. Commun.* 10 (1) (2019) 3447.
- L. Wang, X. Lei, T. Liu, A. Dai, D. Su, K. Amine, J. Lu, T. Wu, Regulation of surface defect chemistry toward stable Ni-rich cathodes, *Adv. Mater.* 34 (19) (2022) e2200744.
- T. Yang, Y. Zheng, Y. Liu, D. Luo, A. Yu, Z. Chen, Reviving low-temperature performance of lithium batteries by emerging electrolyte systems, *Renewables* 1 (1) (2023) 2–20.
- C. Sun, B. Zhao, Z.F. Jing, H. Zhang, Q. Wen, H.Z. Chen, X.H. Zhang, J.C. Zheng, Suppressed electrolyte decomposition behavior to improve cycling performance of LiCoO₂ under 4.6 V through the regulation of interfacial adsorption forces, *Adv. Sci.* 11 (25) (2024) e2309657 (Weinh).
- Z. Bi, Z. Yi, A. Zhang, C. Dong, G. Wang, L. Xie, S. Liao, H. Liu, C. Chen, Z.-S. Wu, A surface-to-bulk tuning deep delithiation strategy for 5C fast-charging 4.6 V LiCoO₂, *Energy Environ. Sci.* 17 (15) (2024) 5706–5718.
- X. Tan, D. Mao, T. Zhao, Y. Zhang, L. Song, Z. Fan, G. Liu, H. Wang, W. Chu, Long-term highly stable high-voltage LiCoO₂ synthesized via a solid sulfur-assisted one-pot approach, *Small* (2022) e220143.
- H.-Z. Zhang, F. Li, G.-L. Pan, G.-R. Li, X.-P. Gao, The effect of polyanion-doping on the structure and electrochemical performance of Li-rich layered oxides as cathode for lithium-ion batteries, *J. Electrochem. Soc.* 162 (9) (2015) A1899–A1904.
- Y. Dong, J. Li, Oxide cathodes: functions, instabilities, self healing, and degradation mitigations, *Chem. Rev.* 123 (2) (2023) 811–833.
- A. Fu, Z. Zhang, J. Lin, Y. Zou, C. Qin, C. Xu, P. Yan, K. Zhou, J. Hao, X. Yang, Y. Cheng, D.-Y. Wu, Y. Yang, M.-S. Wang, J. Zheng, Highly stable operation of LiCoO₂ at cut-off ≥ 4.6 V enabled by synergistic structural and interfacial manipulation, *Energy Storage Mater.* 46 (2022) 406–416.
- Y. Wang, Q. Zhang, Z.C. Xue, L. Yang, J. Wang, F. Meng, Q. Li, H. Pan, J.N. Zhang, Z. Jiang, W. Yang, X. Yu, L. Gu, H. Li, An *in situ* formed surface coating layer enabling LiCoO₂ with stable 4.6 V high-voltage cycle performances, *Adv. Energy Mater.* 10 (28) (2020) 2001413.
- J.-N. Zhang, Q. Li, Y. Wang, J. Zheng, X. Yu, H. Li, Dynamic evolution of cathode electrolyte interphase (CEI) on high voltage LiCoO₂ cathode and its interaction with Li anode, *Energy Storage Mater.* 14 (2018) 1–7.
- J. Hong, H.-D. Lim, M. Lee, S.-W. Kim, H. Kim, S.-T. Oh, G.-C. Chung, K. Kang, Critical role of oxygen evolved from layered Li-excess metal oxides in lithium rechargeable batteries, *Chem. Mater.* 24 (14) (2012) 2692–2697.
- Y. Lu, C.-Z. Zhao, J.-Q. Huang, Q. Zhang, The timescale identification decoupling complicated kinetic processes in lithium batteries, *Joule* 6 (6) (2022) 1172–1198.
- G. Kresse, J. Hafner, Ab initio molecular dynamics for liquid metals, *Phys. Rev. B* 47 (1) (1993) 558–561.
- G. Kresse, J. Furthmüller, Efficient iterative schemes for ab initio total-energy calculations using a plane-wave basis set, *Phys. Rev. B* 54 (16) (1996) 11169–11186.
- G. Kresse, J. Furthmüller, Efficiency of ab-initio total energy calculations for metals and semiconductors using a plane-wave basis set, *Comput. Mater. Sci.* 6 (1) (1996) 15–50.
- P.E. Blöchl, Projector augmented-wave method, *Phys. Rev. B* 50 (24) (1994) 17953–17979.
- J.P. Perdew, K. Burke, M. Ernzerhof, Generalized gradient approximation made simple, *Phys. Rev. Lett.* 77 (18) (1996) 3865–3868.
- G. Kresse, D. Joubert, From ultrasoft pseudopotentials to the projector augmented-wave method, *Phys. Rev. B* 59 (3) (1999) 1758–1775.
- V.I. Anisimov, J. Zaanen, O.K. Andersen, Band theory and Mott insulators: Hubbard U instead of Stoner I, *Phys. Rev. B* 44 (3) (1991) 943–954.

- [47] S.L. Dudarev, G.A. Botton, S.Y. Savrasov, C.J. Humphreys, A.P. Sutton, Electron-energy-loss spectra and the structural stability of nickel oxide: an LSDA+U study, *Phys. Rev. B* 57 (3) (1998) 1505–1509.
- [48] L. Wang, T. Maxisch, G. Ceder, Oxidation energies of transition metal oxides within the GGA+U framework, *Phys. Rev. B* 73 (19) (2006) 195107.
- [49] S. Grimme, J. Antony, S. Ehrlich, H. Krieg, A consistent and accurate ab initio parametrization of density functional dispersion correction (DFT-D) for the 94 elements H-Pu, *J. Chem. Phys.* 132 (15) (2010) 154104.